pOn The Evolution and Form Of Coherent Flow Structures Over A Gravel Bed: Insights From Whole Flow Field Visualization And Measurement

R.J. Hardy[1], J.L. Best[2], D.R. Parsons[3] and T.I. Marjoribanks[1]

[1]Department of Geography, Durham University, Department of Geography, Science Laboratories, South Road, Durham. DH1 3LE, UK

[2]Departments of Geology, Geography and GIS, Mechanical Science and Engineering and Ven Te Chow Hydrosystems Laboratory, University of Illinois, 605 East Springfield Avenue, Champaign, Illinois 61820, USA

[3]Department of Geography, University of Hull, Hull, HU6 7RX UK

Corresponding Author: Richard Hardy
                          r.j.hardy@durham.ac.uk

Abstract

The microtopography of a gravel bed river has been shown to generate turbulent flow structures that originate from shear flow generated in the near bed region. Although field and laboratory measurements have shown that such flows contain a range of coherent flow structures (CFS), the origin, evolution and characteristics of the turbulent structures are poorly understood. Here, we apply a combined experimental methodology using planar Laser Induced Fluorescence and Particle Imaging Velocimetry (LIF-PIV) to measure simultaneously the geometric, kinematic and dynamic characteristics of these CFS. The flow structures were analysed by applying standard Reynolds decomposition and Lagrangian vortex detection methods to understand their evolution, propagation and growth in the boundary layer, and characterize their internal dynamical complexity. The LIF results identify large, individual, fluid packets that are initiated at the bed through shear that generate a bursting mechanism. When these large individual fluid packets are analysed through direct flow measurement, they are found to contain several smaller scales of fluid motion within the one larger individual fluid parcel. These flow measurements demonstrate that near-bed shear control the initiation and evolution of these CFS through merging with vortex chains that originate at the bed. These vortex chains show both coalescence in the formation of the larger structures, but also the shedding of vortices from the edges of these packets, which may influence the life-span and mixing of CFS in open channels. The lifespan and geometric characteristics of such CFS are critical in influencing the duration and intensity of near-bed stresses that are responsible for the entrainment of sediment.

Key words

Coherent Flow Structures, Gravel Bed Rivers, Turbulence

1. Introduction

One key feature that determines the characteristics of river flow is its interaction with a heterogeneous sedimentary bed, which creates shear instabilities in the boundary layer that are often invoked as the mechanism in the formation of macroturbulent (i.e. flow-depth scale) flow structures [*e.g. Kostaschuk and Church,* 1993*; Bennett and Best* 1995*; Venditti and Bennett,* 2000*; Best and Kostaschuk,* 2002*; Jessup et al.,* 2013]. These shear instabilities are generated by flow separation induced by boundary layer flow over multi-scale bed topography [*Wiberg and Smith*, 1991; *Dinehart*, 1992; *Robert et al.,* 1992; *Buffin-Bélanger and Roy*, 1998; *Lacey and Roy*, 2006; *Hardy et al.*, 2007, 2009], and through the wakes of individual topographic protrusions and jetting of higher-velocity flow between such bedforms. These turbulent flows are characterized by the interactions and coalescence between flow structures of different sizes and origin, which are formed by several superimposed means of turbulence production [*Roy et al.,* 1999; *Nikora and Roy*, 2012]. River turbulence is therefore not a random field, and it has been shown that it is possible to decompose complex, multi-scaled, quasi-random flow fields into elementary organized structures that possess both spatial and temporal coherence [*Adrian,* 2007]. These structures are inherently three-dimensional, where at least one fundamental flow component exhibits correlation with itself, or with another flow component (or product of), over a range of spatial and/or temporal scales [*Robinson*, 1991; *Roy et al.,* 2004; *Adrian*, 2007; *Nikora and Roy*, 2012]. These turbulent structures are known as eddies [*Townsend*, 1976] but are more commonly referred to as coherent flow structures (CFS) [*Cantwell*, 1981; *Adrian*, 2007, 2013; *Venditti et al.,* 2013], and it is their make-up that ultimately control the structure of turbulent flows.

CFS in shallow geophysical flows over rough surfaces have been previously studied [e.g. *Vendetti et al.,* 2013], and appear similar to flow structures observed over smooth boundaries. As such, definitions proposed in classical boundary layer hydraulics [*Cantwell, 1981; Robinson,* 1991*; Adrian,* 2007*; Adrian and Marusic* 2012] have been widely adopted. In general, CFS are defined as elementary organized motions that are considered as individual entities if they exist for long enough to be observed using flow visualization, and as such they

possess temporal coherence [*Adrian,* 2007] and/or contribute significantly to the mean flow and other properties, including turbulent kinetic energy and Reynolds stresses [*Adrian and Marusic,* 2012]. These flow structures may contain ir/rotational parts [*Adrian and Marusic,* 2012], but spatial coherence is not a sufficient characteristic to define an organized motion [*Adrian,* 2007]. As such, CFS are the building blocks of turbulent flows; they are detectable by a common topological pattern and they are recurring [*Adrian and Marusic,* 2012].

Macroturbulent motions in rivers have regularly been identified [*Jackson*, 1976; *Babakaiff and Hickin,* 1996; *Muller and Gyr*, 1982; *Best*, 2005b*; Horner-Devine et al.*, 2013; *Marquis and Roy*, 2013]. They have a quasi-cyclic pattern, with ejected low-momentum fluid from a burst in the bed region growing until a size equal to the flow depth, while high-momentum fluid moves from the outer flow down to the bed which influences the entire flow field [*Grass,* 1971; *Talmon et al.*, 1986; *Yalin,* 1992*; Shen and Lemmin*, 1999; *Best* 2005a]. These turbulent motions generate rolling structures [e.g., *Klaven*, 1966; *Klaven and Kopaliani*, 1973; *Imamoto and Ishigaki*, 1986 a&b] that scale with the flow depth (h) in the vertical and in the order of $2h$ in the lateral direction [*Zaitsev*, 1984]. In gravel bed rivers, the downstream scale of these structures scale with both the hydraulic roughness and flow conditions: the greater the flow Reynolds number, the more pronounced the development of the CFS [*Shvidchenko and Pender*, 2001] that scale between 4 to $7h$ in the downstream direction, with this scale inversely proportional to the bed roughness [*Klaven*, 1966; *Klaven and Kopaliani*, 1973; *Shvidchenko and Pender*, 2001]. The average frontal angle of the CFS has been shown to be between 36° and 45° [*Buffin-Belanger et al.,* 2000*; Hardy et al.,* 2009] with the upstream slope of the structures increasing with flow Reynolds number. This process occurs over a distance of $6h$ [*Shvidchenko and Pender*, 2001] as these structures are not permanent. The eddies become unstable with the shedding of smaller vortices which changes and redefines the boundaries of the large-scale structures [*Hardy et al*., 2011].

Although CFS have frequently been observed, a complete understanding of both their generation and evolution is limited, even though they ultimately form the nature of turbulent river flows. Furthermore, these structures contribute to both the Reynolds stresses and turbulence intensity [*Vendetti et al.,* 2013], which implies the initiation of movement and transport of sediment will be linked to such structures [*Drake et al.,* 1988*; Hardy,* 2005*; Garcia et al.,* 2007*; Diplas and Dancy,* 2013; *Singh and Foufoula-Georgiou*, 2013] and they will also influence both suspended sediment [*Heathershaw,* 1974; *Bai et al.,* 2013] and bed load [*Jackson,* 1976; *Schmeeckle et al.,* 2007] transport. This incomplete understanding thus

impedes our ability to predict the boundary layer dynamics at the micro-scale. It is suggested herein that part of this underdeveloped understanding of CFS stems from our inability to measure and detect the origin and evolution of these structures. The aim of the present work is to apply a combined visualisation and measurement methodology to examine the evolution and growth of CFS in the near bed region, and then subsequently quantify their internal dynamical complexity and temporal characteristics.

2. Previous studies to understand coherent flow structures in gravel bed rivers

Flow visualization has often been applied to improve our understanding of turbulence [*Van Dyke,* 1982] as it provides a description of the flow by tracking individual turbulent structures. Flow tracers have been applied in natural rivers to understand turbulent flow over gravel surfaces [*Roy and Buffin-Belanger,* 2001*; Paiement-Paradis et al.,* 2003] and such studies have provided considerable insight into the geometric characteristics and the size and spacing of these CFS. However, critically, this approach does not allow the measurement of the flow within individual CFS and the surrounding fluid.

The flow velocity measurements required to understand CFS are practically more complicated than flow visualization. One approach has been the use of multiple flow meters to provide an Eulerian measurement of the flow. These studies have identified large-scale flow structures formed by interaction with the bed [*MacVicar and Roy,* 2007*a&b; Lacey and Roy,* 2008], which were detected through turbulent wake statistics [*Lacey and Roy,* 2008]. These data confirm flow visualisation analyses, showing a spatial scaling of the CFS with flow depth [*Marquis and Roy,* 2006], while time series analysis has shown that these flow structures follow a power function that equates to a bursting cycle [*Paiement-Paradis et al.,* 2003].

Whole flow field measurements at millimetre scale spatial resolution and Hertz scale temporal resolution may be obtained through particle imaging velocimetry (PIV) in flume experiments [*e.g. Best, 2005a; Cooper and Tait,* 2008; 2010 *a&b; Hardy et al.,* 2009, 2010]. Analysis of this type of data has typically been accomplished through standard Reynolds decomposition [*Hardy et al.,* 2009; 2011] or double-averaging to quantify both the spatial patterns in the mean flow quantities [*e.g. Cooper and Tait,* 2010a] and the contribution of these CFS to the Reynolds-averaged statistics [*Adrian,* 2007]. However, the identification of individual structures is subjective [*e.g. Hardy et al., 2009*].

Although flow visualisation, single-point and whole flow field measurements have all led to a new understanding of CFS, there has necessarily been a degree of subjectivity in these interpretations. It is suggested herein that in order to understand fully the characteristics of CFS, it is necessary to simultaneously visualize and quantify the flow characteristics. Herein, we employ a methodology, originally reported in *Hardy et al.* [2011], to quantitatively and simultaneously examine the flow characteristics of CFS over a gravel surface. This approach applies a combined particle imaging velocimetry (PIV) and laser induced fluorescence (LIF) methodology that enables measurement at a temporal resolution of 50Hz and a spatial resolution of millimetres. This approach allows us to examine the propagation and evolution of CFS while quantifying the full details of the overall flow characteristics. These data provide a whole flow field insight into the localised flow structures that are present through the evolution of the CFS, and how these structures evolve and finally break up. Such a process understanding provides insight into the boundary layer dynamics and an indication of the forces acting on the river bed morphology.

3. Experimental methodology

The experiments were conducted in a flume 10 m in length (l_c) and 1 m in width (w). The slope of the flume was adjusted to achieve a constant flow depth along the test section, which was located 5.5 m downstream from the channel inlet. A bulk sample of gravel ($D_{50} = 0.044$ m, $D_{84} = 0.064$ m) was water worked to form a stable bed (Figure 1a). The bed topography was measured using a terrestrial laser scanner (Figure 1b) that provided a digital elevation model (DEM) at a 5 mm resolution (accuracy ± 1 mm). The effective roughness characteristics of the surface were calculated from the DEM following the approach of *Hardy et al.* [2010], which derives a scale-dependent roughness value determined from the 84th percentile (R_{84}) of the elevation differences between points as a function of horizontal scale. To maximise the sample size, a distance of $w/2$ was used, which yielded a constant R_{84} of 0.04 m over a search distance of 0.2 m.

A water depth of 0.3 m above the flume bed was used for two principal reasons. Primarily, flow in gravel bed rivers is shallow, with the ratio of mean depth to effective roughness height (h:D_{50}) often being less than 10–20 in flood conditions and less than 5 during base flow conditions [*Charlton et al.,* 1978*; Bathurst,* 1978]. Secondly, this water depth was used to ensure that the flow width to depth ratios were high enough to reduce possible turbulence

anisotropy and stream-wise secondary circulation [*Colombini,* 1993], although streamwise secondary circulation has been observed under similar hydraulic conditions [e.g. *Rodríguez and García* 2008*; Tamburrino and Gulliver* 1999*; Tominaga at al.* 1989]. Four different flow velocities were investigated (Table 1) to provide a range of Reynolds numbers between 19 000 and 132 000 and Froude numbers between 0.04 and 0.44, thus the flow was fully turbulent and subcritical. These hydraulic conditions were used for theoretical and practical reasons. Theoretically, flow in a river is unsteady and it is therefore necessary to assess how turbulence characteristics change under different flow conditions, while practically it was necessary to ensure that sediment was not entrained to prevent damage to the experimental facility.

3.1. Velocity measurements

Velocity measurements were collected using a two-dimensional time-resolved PIV. The PIV methodology and post-processing applied herein are identical to that previously reported by *Hardy et al*. [2005; 2009; 2010; 2011]. The laser was mounted underneath the flume and orientated vertically, with the flume illuminated through a window 2 mm wide and 0.3 m long in the base of flume. A Litron Nano laser was used in single-pulse mode to maximize field-of-view illumination and the system was set to collect data at a temporal resolution of 50 Hz (each laser pulse providing ~100 mJ at 50 Hz). The PIV camera (pixel resolution of 1280x1024) was located perpendicular to the flume walls, so flow could be imaged to quantify the downstream (u-) and vertical (w-) components of flow velocity. To derive the velocity vector map, an interrogation region (16×16 pixels, where 1 pixel $\approx 2.5\times10^{-4}$m) was overlain over the images. For each interrogation region, in each pair of images, the displacement of groups of particles between the first and second image was measured using a fast Fourier transform (FFT) based spatial cross-correlation technique and a velocity vector was determined [*see Westerweel*, 1997]. This methodology allowed data collection at a spatial resolution of 2×10^{-3} m. In order to maximize the signal-to-noise ratio of the particle cross-correlations in the PIV analysis, a sequence of six quality checks [*see Hardy et al.,* 2005] was undertaken. Applying this methodology, the estimated precision of the derived velocities was greater than 1/10th of a pixel [*Wilbert and Gharib,* 1991] and the uncertainty in the velocity measurements was therefore less than $\pm$ 0.08 mm s^{-1}. The field of view interrogated by the PIV covered a region of 0.3 m x 0.25 m in the downstream and vertical planes, with the region of flow interrogated demonstrated in Figure 1b.

The PIV set-up provides a view of the whole flow field view as demonstrated by the downstream (u-) component for the Re 132 000 experiment (Figure 1c). The time-averaged flow field shows the influence of the bed topography on the near-bed flow, with a large region of recirculation in the wake of protruding clast similar to the results reported previously by *Hardy et al.* [2009]. Above this clast, the average flow velocity increases with depth and, although individual CFS are not identified in this time-averaged plot, the effect of the topographic protrusion is seen to influence the near bed flow. In addition, when a turbulence intensity profile is studied (calculated using the RMS value of each velocity component) for the Re 132 000 experiment (Figure 1d), a region of highly turbulent flow in the near-bed region (<0.3 z/h) is detected. This is in agreement with previous work on flows over gravel beds at high-flow Reynolds numbers that has shown a region of higher turbulence intensity between 0.2 and 0.5 z/h [*Hardy et al.,* 2009; 2010], which is formed through skimming flow [*Grass*, 1971; *Grass et al.,* 1991; *Krogstad et al.*, 1992] generated over the largest clast and wake flapping [*Nowell and Church*, 1979].

3.2. Measuring the flow structures

In order to visualise and subsequently measure the CFS, Laser Induced Fluorescence (LIF) was applied, with the full methodology being reported in Hardy *et al.* [2011]. In the present study, a fluorescent tracer, Rhodamine 6G (Rh6G) diluted in de-ionized water, was fed through a 4 mm tube using a peristaltic pump, and introduced through the bed and entrained into the flow (Figure 1e). The peristaltic pump ensured the flow of the Rhodamine dye was the same as that of the flow at the bed in order to prevent any added momentum that may influence the characteristics of the CFS [*Roy et al.,* 1999]. The laser illuminated the tracer within the measurement field of view and allowed visualization of the turbulent structures within the flow (Figure 1 e&f) and measurement of flow. Care was taken not to add too much Rhodamine, as over-illumination affected the quality of structure detection and PIV measurement. Through the use of a second camera, the LIF was run concurrently with the PIV, although a square-notch green filter was installed on the PIV camera lens to remove light of the LIF wavelength (450–575 nm for Rhodamine 6G) from the PIV images. This provided a simultaneous two-dimensional (downstream (l) and vertical (h)) visualization and flow measurement of the CFS.

Here, the LIF image was used as a structure mask. Standard image processing techniques were used to convert the LIF image (Figure 1f) into a binary image (Figure 1g). This was achieved by applying the algorithm of *Otsu* [1979] so that the large-scale geometric characteristics were identified. This process provided a binary mask for detection and delineation of coherent flow structures (Figure 1g) that initially enabled the geometric characteristics of individual flow structures to be investigated, but subsequently was overlain on the PIV data to allow extraction of the flow data.

It must be recognized that there is an inherent limitation with this approach in that we are applying a static two-dimensional technique to try to capture a dynamic complex three-dimensional structure that grows over space and time. Since the technique is thus reliant on the CFS passing through the laser sheet ($\approx$ 2mm wide), there is a probability that the CFS originates outside the field of view and there may be a degree of lateral interaction with adjacent CFS. We sought to minimize this effect as much as possible by feeding the Rhodamine in front of the most protrusive roughness element (Figure 1e, PCl) in order to minimize such concerns.

4. Methods of Analysis

The analysis methodology was designed following the definition of a CFS outlined above, in which such structures possess both temporal and spatial coherence, contribute to the mean flow, and contain turbulent kinetic energy and ir/rotational components (vorticity) [*Adrian and Marusic,* 2012; *Venditti et al.,* 2013]. The LIF data also provided a structure mask to distinguish the flow structure from the surrounding flow. Flow data collected with PIV was analysed in several ways. Firstly, quadrant analysis was applied [e.g. *Lu and Willmarth*, 1973; *Bogard and Tiederman*, 1986; *Bennett and Best*, 1995] to discriminate the boundary layer turbulent events that initiate and cause growth of the CFS. This approach was applied once stationarity in the velocity times series had been determined using the cumulative variance approach [e.g. *Sukhodolov and Rhoads,* 2001], thus allowing time averaged means to be calculated. Secondly, the turbulent kinetic energy was calculated to evaluate flow within the CFS and how this compared to the surrounding flow. Thirdly, two-dimensional (*x-z*) vorticity was calculated to assess the ir/rotation of the structures, and to detect coalescence or vortex shedding. Vortex detection was then extended by application of the Finite-Time Lyapunov Exponent (FTLE) method [*Haller,* 2001*; Green et al.,* 2006]. Lyapunov exponents

have previously been used to study the chaotic nature of a dynamical system [*Sprott*, 2003], and have also been used in identifying vortices within flows as they calculate trajectories either forwards or backwards in time. When projected backwards, as they are in the present study, the FTLE detects regions of the flow that act as attractors within the flow [*Haller and Yuan*, 2000]. Regions of high FTLE identify vortices that have been classified as Lagrangian coherent structures (LCS) [*Haller*, 2000; *Haller and Yuan*, 2000]. Thus, the FTLE method has been applied in this study to detect the evolution point and growth of the flow structure, and by applying backward projection over different time periods provide an indication of its temporal coherence.

In the next section, each experiment is referred to with reference to the Reynolds number of the flow conditions; i) 19 000; ii) 46 500; iii) 87 000 and iv) 132 000. Initially, a time series of an evolving structure is analysed in order to understand the evolution and growth of these structures. This time series is taken from the Re 132 000 experiment as previous work has shown CFS are more pronounced as the Reynolds number increases [*Shvidchenko and Pender*, 2001; *Hardy et al.*, 2009]. For the other three Reynolds numbers, a different approach is applied where five structures are identified for each flow condition that display similar geometric characteristics to those previously observed [e.g. *Lacey and Roy,* 2006; *Hardy et al.,* 2011]. This approach has been applied to assess the range of different structures that have entrained Rhodamine and follows the observation of *Adrian and Marusic* [2012] that CFS are recognizable, despite randomness, by their common topological patterns.

5. Results

5.1. A time series of an evolving flow structure.

A series of five images, each 0.06 seconds apart, were identified from within the Re 132 000 experiment (Figure 2, labelled T1 to T5, in increasing time). Initially, the flow structures characteristics are identified (Figure 2, row 1) and then the flow dynamics are analysed through quadrant analysis (Figure 2, row 2), and then by examining both turbulent kinetic energy (Figure 2, row 3) and vorticity (Figure 2, row 4).

The geometric characteristics identified in the LIF image T1 show that the Rhodamine is entrained into the shear flow generated by the topographic protrusion (labelled A). This lifts the structure into the flow with a leading edge at approximately 45˚ (labelled with a white dashed line). The structure does not fill the whole field of view in this short time period,

although the entire length of observation is less than 0.5 seconds. This leading edge decreases in angle with time as the structure moves through the field of view ($\approx 35°$ in T4, labelled with a white dashed line), although the ability to detect the structure appears to decrease due to the dilution / oxidation of the Rhodamine. Finally, the periodicity associated with this process can be estimated in T5 where the next structure is starting to generate over the topographic protrusion (A) behind the initial structure (both marked with yellow dotted lines).

The PIV measurements allow the internal flow dynamics of the structures detected by LIF to be characterised. The most apparent observation is that although the LIF detects an individual fluid parcel through space and time, the PIV measurements identify several smaller units of fluid exist within the one larger individual fluid parcel. The instantaneous non-thresholded (i.e. by any mean Reynolds stress hole size [*Lu and Willmarth*, 1974]) quadrant plots are shown (Figure 2, row 2). Just upstream of the detection region of the LIF, Q1 (outward interaction) events are detected over the topographic protrusion A (circled, in T1), which have previously been shown to be the most efficient, although least common, structure in entraining sediment [*Nelson et al.,* 1995]. However, in the immediate leeside of the protrusion, where the flow structure is detected, the flow is dominated by Q4 (sweep) events, and as such the majority of the structure (>80%) consists of Q4 events. The secondary flow structure, in terms of total spatial coverage, contained within these structures is Q1 events that are located both at the base and the top front (tip) of the structure. This observation is consistent for all five time images. Directly above the flow structure, a packet of Q2 (ejections) events exist from T2 onwards (circled in T2 column). This suggests flow is initially suppressed in the near-bed region and this would agree with the flattening of structure observed in the LIF images. However, since the parcel of fluid above the structure is moving (lifting) away from the bed, this implies that the local pressure is reduced, thus allowing the structure to lift and develop, as has been shown previously in the shear layer through absolute and convective instabilities [*Socolofsky and Jirka*, 2004].

When the turbulent kinetic energy (TKE) is analysed (Figure 2, row 3), high TKE can be observed in the base of the structure as it passes over topography (marked with a box). Within this box just along the top edge of the structure high TKE (> 0.005 m^{2}s^{-2}) is detected as well as a chain of higher TKE (≈ 0.003 m^{2}s^{-2}) between the source of the structure and the structure which leaving the box. This is potentially generated through shear, although the intensity of the TKE appears to diminish with distance away from the bed (marked with arrow (Figure 2, row 3, column 2). This same mechanism can be observed to be occurring again

(Figure 2, row 3, column 2, behind arrow) although on this occasion no Rhodamine is entrained. However, the CFS does appear to follow certain trends. Initially, the LIF dye appears to have been entrained at the end of a large structure that has passed through that point. In Figure 2 (T2), a region of high TKE is marked (dotted ellipse) that has a geometrically similar shape to the large structure (extending up to 0.5 z/h) that the LIF appears to be following (T2 marked with upper arrow). Secondly, as demonstrated in column T3, a region of high TKE that is moving towards the bed is located downstream of the structure, as demonstrated by the quadrant analysis.

The vorticity plots (Figure 2, row 4) show regions of either very strong negative or positive rotational components within the structure. The most obvious observation, and one that is also in agreement with the quadrant analysis, is that the flow structure is not a single unit of homogenous flow but has several localised packets of flow. Furthermore, the top of the structure appears in some cases to contain packets of fluid of negative vorticity (anticlockwise rotation), while at the bottom of the structure there is a prominence of structures with a positive vorticity (clockwise rotation) (see T3, labelled with 2 arrows). This implies that smaller vortices are shearing off the back of the larger structures, while at the bed smaller vortices are also being sheared through shear interaction with the bed.

Vortex detection is undertaken by applying FTLE with structures tracked backwards in time for 0.05, 0.5, 1 and 2 seconds for time frames T1, T3 and T5 (Figure 3). In these images, the structure is coloured black to analyse the flow surrounding the structure, whilst white regions show a non-calculation. This non-calculation occurs where the temporal track-back time were too great and would have required velocity measurements outside of the field of view to make a successful calculation. At the shortest track-back period (0.05 second, row 2), high FTLE values identify a series of vortex chains. These structures all originate at the bed and have a similar trajectory (lead angle of ≈ 45˚) to those structures identified with the Rhodamine. Furthermore, high FTLE values exist throughout the flow (an example is marked with a dashed line, row 2 on T5), and detect vortex chains that may have been generated from topographic protrusions outside the field of view. However, the high FTLE values with a track-back time of 0.05 seconds do not coincide with the structure, but there appears to be a high FTLE band on either side of the structure (labelled in T3 with two dashed lines). Following the observations made from the analysis of vorticity (Figure 2, row 4), these bands potentially depict the vortices shearing off the back of the structure or being sheared off through interaction with the bed.

When a 0.5 second track-back time is applied, high FTLE values again detect several vortex chains that can be seen to have a trajectory with a lead angle of ≈45˚. With an increase in the temporal track back period, the high FTLE values and spatial locations of the LIF structure appear to correspond with the structures following defined paths (marked with a line in T3), with the LIF being entrained by vortex chains originating at the bed. This observation is confirmed when a 1-second track-back time is applied (Figure 3, row 4, T1, & 3 marked with dashed line) with the flow moving away from the bed. By image T5, the gradient of the front angle has increased as it moves further into the boundary layer. The pattern is more difficult to detect when a 2-second track-back time is applied. This is a function of the size of the field of view and the speed of flow. However, there does appear to have some spatial connection, with the high FTLE attractors within the structure contained within a parcel of flow (in front of the structure in T1 and overlapping the structure in T3 marked with dashed oval). Complete overlap with high attractors may be a function of entrainment but does potentially show both the spatial location of the origin of the structure and, as a factor of the track back periods, an indication of the temporal coherence.

The FTLE demonstrates that all the vortex structures start at the bed following a lead angle of ≈35˚ to 45˚. For shorter track-back periods, the flow structure appears to sit on high FTLE attractors, which could either imply that small structures, as identified in the vorticity, are spinning off, or secondly that the structures follow predefined flow paths from topographic protrusions from the bed.

5.2. Analysing individual structures

In the following section, CFS from the other three Reynolds numbers are examined. However, instead of analysing a time sequence, individual structures have been analysed to assess whether they possess similar geometric or kinematic characteristics.

5.2.1. Geometric characteristics of flow structures.

The individual CFS elucidated at the three Reynolds numbers through LIF are presented in Figure 4 as post-processed images (as discussed in section 3.2). The first observation for all these identified flow structures across the three Reynolds numbers is, as with the Re 132 000 experiment, that none of the CFS grow to their full size within the field of view, with the

maximum height of any structure identified in the flow ≈ 0.4 *z/h*. Furthermore, no classical geometric structure can be identified that clearly scales with the flow Reynolds numbers. It is, however, suggested that the structures are not the size of the flow depth due to the experimental methodology employed. In particular, the location of the LIF infeed was likely too close to the PIV field of view, and thus the structures into which the dye was entrained did not have the spatial distance to evolve fully. However, this limitation was necessary for two experimental reasons: i) these structures are fully three-dimensional and herein a two-dimensional PIV/LIF measurement technique is being applied. It is therefore necessary to ensure that the Rhodamine dye passes through the PIV laser sheet for illumination and thus the feeder tube needs to be close to the field of view; ii) the concentration of Rhodamine needs to be carefully monitored to prevent either over-illumination, and thus a reduction in the quality of the PIV data, or the oxidation or dilution of the Rhodamine that would reduce the possibility of detection.

For the Re 19000 experiment (Figure 4, column 1), a series of trends can be observed. Primarily, the CFS can be seen to be entrained in the near-bed region (Figure 4a, *i*) with the body of the structure moving higher in the flow, and with some positive rotation of the structure at its front underside (see arrow in Figure 4a in front of structure). A similar CFS which has moved further into the field of view (Figure 4b, marked with arrow), appears to have been squeezed into a narrower shape with smaller structures (vortices) being shed from the bed. This squeezing of the CFS is likely associated with the main shear layer formed from the largest protruding clasts, as previously discussed by *Hardy et al.* [2010]. These CFS are not found in isolation but rather a sequence of structures can be identified, such as in Figure 4c where two similar CFS are found in sequence (separated by a dotted line ii). Finally, as more dye enters the field of view (a problem encountered at lower flow velocities), these similar structures are identified in the left hand side but structures with a streaky nature appear above the shear layer (Figure 4e, arrow iii).

The CFS identified for the Re 46 500 experiment show similar geometric characteristics to those identified for the Re 19 000 experiment, with a sequencing of small structures (Figure 4g), located in the near bed region and experiencing shear flow. However, larger structures are also detected (Figure 4i & j) that are clearly generated in the near-bed region and appear to be ejected low-momentum fluid (Figure 4i, arrow iv). Here, the CFS initially appears to be supressed below the shear layer and then moves up and through the shear layer (0.5 *x/l* in Figure 4i), with a frontal angle of approximately 45°, and potentially with vortices shedding

off the back of the structure. Behind this CFS, a streaky structure is observed as identified previously. This type of structure is again identified as the Reynolds number increases in the Re 87 000 experiment (Figure 4 k-o were similar geometric structures are identified. The structures are supressed within the near-bed region and move upwards at a shallow angle of 25° (Figure 4k, marked with arrow). In all these visualizations, none of the detected structures are an isolated closed entity, but rather are comprised of several CFS identified by the LIF structures, that appear to either shear off the back of, or be entrained into, the principal CFS.

5.3. *Flow within individual structures and surrounding flow*

The same analysis sequence detailed above was applied where the flow within the structure and in the surrounding flow is analysed. As with the Re 132 000 experiment, the most apparent observation is that although the LIF detects an individual fluid parcel through space and time, there are several smaller parcels of fluid within the one larger individual CFS.

5.3.1. *Quadrant Analysis*

The non-thresholded instantaneous quadrant plots for the Re 19 000, 46 500 and 87 000 experiments (Figure 5) are shown with the quadrants contained within the structure in bold and the surrounding flow translucent. If the overall flow field is considered first, for Re 19 000, the majority ($\approx 70\%$) of the field of view is comprised of Q2 (ejection) and Q3 (inward interaction) events (with the exception of Fig. 5d), although there is no real defined spatial pattern. Q4 (sweep) and Q1 (outward interaction) events are also observed, although they are fewer and are typically found lower in the flow. However, the Q4 structures do detect a flow structure that is geometrically similar (Figure 5c, marked with eclipse) to the previously identified structures (e.g. Figure 1g) (i.e. the lead angle of the structure is $\approx 45°$ located in the near bed ($z/h < 0.4$)), although they are not detected by the entrained Rhodamine. As the Reynolds number increases, there is a clear increase in Q4 events. For the Re 46 500 experiment, these Q4 events are contained in small packets of fluid with the size of the fluid packets increasing, and possibly becoming more coherent, as the Reynolds number increases in the Re 87 000 experiment. However, across all Reynolds numbers, , the majority of the flow contained within the CFS detected by the Rhodamine consists of Q4 events with Q1 events located both at the base and the top front (tip) of the structure.

5.3.2. Flow within individual flow structures

The turbulent kinetic energy (TKE) is calculated for every image and shown in Figure 6. The results are presented in an identical manner to the quadrant analysis where the structure is shown in bold while the turbulent kinetic energy in the surrounding flow is translucent. It is evident that, over the range of Reynolds numbers investigated, the macro turbulent structures identified in the LIF are generally located in regions of low turbulent kinetic energy, although, as in the Re 132 000 experiment, there are units of high TKE within these structures. The region of low TKE where CFS are detected is shown by two parallel dashed lines on Figure 6 for the 3 examples (Figure 6 *a,b,l*).

A consistent pattern is found for the Re 19 000 experiment (Figure 6 a-e). The CFS detected by the Rhodamine dye is located within a region of low TKE (Figure 6 a & b (marked within a pair of parallel dashed lines) and Figure 6e (within ellipsoid)). It is clear that on either side of this region, the TKE is higher than that contained within the flow structure. A similar observation can be made for the Re 87 000 experiment (Figure 6l marked with parallel dashed lines) or in Figures 6n and 6o, where the structure is located within a region of low TKE. The opposite of this pattern appears for the Re 46 500 experiment, where the structure is generated from, and moving above, the shear layer (labelled in Figures 6g and 6i with an arrow and the parcel of fluid above shear layer marked on Figure 6h with an ellipse). It is also apparent that the TKE is lower in magnitude than the surrounding fluid (Figure 6h) as the structure has already moved out of the shear layer. This highlights that these CFS are being generated by localised shear, where they are potentially entrained into, or coalesce with, other turbulent structures that are moving upwards out of the flow.

5.4. Two dimensional (x-z) vorticity

Two dimensional (*x-z*) vorticity for each image is shown in Figure 7. In general, all the CFS across the range of Reynolds numbers possess weak positive vorticity, showing a rolling motion generated from shear with the bed. However, closer inspection shows that each structure is not a single homogeneous flow structure, but rather comprises several vortices of both rotating and counter-rotating flow. When the Re 19 000 experiment is considered, the general positive vorticity demonstrates that the structure is lifting up into the flow. However, localised packets of high intensity vorticity can be observed (Figure 7a, region i & Figure 7d, region ii). At this low Reynolds number, these packets do not visually occupy more than 10%

of the whole structure, although there is an apparent sequencing of events with the high positive motion directly next to values of high negative vorticity. A similar pattern is observed for the Re 46 500 experiment (Figure 7f, region iii and Figure 7h, region iv) where regions of positive rotating flow are mixed with anticlockwise-rotating flow. These local units become more dominant at this Reynolds number, cover a greater spatial area (approximated to be 20% of the structure) and are located close to the top front of the structure. Here, the tip of the structure is rotating forward and lifting into the flow, but directly behind this the flow is rotating in the opposite direction, with smaller structures either shearing off the back of the structure or being entrained into the structure. However, this characteristic is not apparent in the Re 87 000 experiment.

The vorticity analysis demonstrates that the CFS have a positive rotational structure, but are not single homogenous units and are comprised of both ir- and rotational parts, thus agreeing with the observations of *Adrian and Marusic* [2012]. It is unclear from the present analysis whether the localised high intensity vorticity within the CFS is either entrained from the shear layer as the structures grow, or whether the structures are becoming unstable and transferring their energy to smaller eddies. This latter behaviour would follow the model of *Falco* [1991], where the shedding of smaller vortices reforms and redefines the boundaries of the large-scale motions on which they develop [*Hardy et al.*, 2011].

5.5. Vortex detection through Finite-Time Lyapunov Exponents (FTLE)

In the application of FTLE herein, the starting time frames to track back the flow structures are those images displayed in Figure 4. In order to capture all the flow structures three different track-back periods were applied (0.5, 1, and 2 s). A 0.05s track back period was not applied as this has been demonstrated to be too short a period in the observations made in Figure 3. Furthermore, in order to demonstrate the results, only 1 image for each Reynolds number is presented in Figure 8.

When the Re 19 000 experiment is examined (Figure 8, row 1), the vortex chains that originate from the bed are apparent, as are some flow structures higher in the flow that are suggested to originate at the bed, but upstream of the field of view. Again, high FTLE values correspond spatially with the LIF (marked Ai and Aii on Figure 8, row 1) as the flow structure moves downstream. Although the geometry of the CFS used for the Re 46 500 analysis is different, (Figure 8, row 2), for the three track-back periods (0.5, 1 and 2 seconds),

high FTLE values can be observed in the flow, although the best agreement in terms of spatial location between the FTLE and the CFS detected in the image is for the 2-second period. There is a strong band of FTLE (labelled Bi) which shows a vortex chain that has entrained the region of LIF. Agreement with a 1-second track-back is poorer, although there is a region of high FTLE at the front of the structure where the LIF is slightly below a band of high FTLE (Bii). The same characteristic can be seen for in the Re 87 500 experiment where the CFS corresponds with a region of high FTLE (marked Ci), but again weak agreement is present with the 1-second FTLE. A second observation that can be made for the 2-second track-back period is that a secondary band of high FTLE is present over the topographic protrusion (labelled Cii), perhaps demonstrating a periodicity in the processes. Again several small vortices are detected in the 0.5-second FTLE.

6. Discussion and Conclusions

This study has examined the nature of turbulent flow over a gravel bed at four different Reynolds numbers by applying a combined measurement and flow visualisation technique. This has enabled the geometric and dynamic characteristics of the CFS to be measured at a millimetre-Hertz spatio-temporal scale. This technique allows us to improve our understanding of the contribution of CFS to the turbulent flow, the generation of bed shear stresses and transport of sediment over gravel beds. From this analysis, a new conceptual model of flow structure evolution, growth and decay over a gravel bed is presented (Figure 9).

The LIF analysis identifies flow structures that are individual entities and similar to the field observations of Roy *et al.* [2004]. These CFS persist for a sufficient temporal period to be observed in flow visualization and therefore fulfil one of the criteria proposed by *Adrian* [2007]. Furthermore, these structures are reoccurring and are identifiable, despite randomness, by their geometric characteristics [*Adrian and Marusic,* 2012]. These results also confirm that the CFS are generated by a process akin to the 'bursting' cycle (Figure 9a) [*e.g. Grass* 1971*; Grass et al.,* 1991*; Nezu and Nakagawa,* 1993] where ejections force relatively low-momentum fluid away from the bed, although these upwellings are linked to shear layers formed by flow over protruding topography. These CFS have similar geometrical characteristics to those previously deduced from flow measurements, with frontal angles between 36° and 45° [*Buffin-Belanger et al.,* 2000*; Hardy et al.,* 2009], and thus appear

similar in nature to roller vortices formed in a classical boundary layer [*Adrian*, 2000]. However, previous work has suggested that such structures grow until they are nearly equal to the flow depth [*Grass*, 1971; *Shvidchenko and Pender,* 2001], which is not observed in the present experiments. Three reasons may be forwarded to explain this anomaly. First, if the experimental conditions are compared with previous experimental work (Table 1), it is clear that both the bed particle size and flow depth used herein are an order of magnitude greater than previous experiments, although the relative submergence of clasts (D_{50}/h) is the smallest. Furthermore, although the Reynolds numbers are comparable the Froude numbers are low compared to the previous experiments. Thus the processes observed previously may not scale with these extremely rough beds under these flow conditions. Secondly, this lack of correspondence between past work and the present results may be associated with the fact that the field of view is too small to view the complete cycle, as in the present experiments the field of view is $\approx 1h$. Finally, there is the possibility that inrushing fluid into the top of the CFS may dilute the Rhodamine making the detection of the top of the structure problematic.

The bursting cycle revealed by the LIF was quantified by applying direct flow measurement. Although the LIF identified individual fluid packets moving through space and time, these structures were found to comprise several smaller parcels of fluid within the one larger CFS (Figure 9). This nesting of different scale flow structures may reflect either the process by which the structures are formed (e.g. coalescence) or the fact that these structures are not permanent and a cycle occurs over a distance of $6h$ [*Shvidchenko and Pender*, 2001] with vortices being shed off the back of the CFS [*Falco*, 1991]. The instantaneous, non-thresholded, quadrant analysis demonstrates that as the flow Reynolds number increases there is an increase in the percentage of the flow field containing Q4 events (Figure 9). At lower Reynolds numbers, these Q4 events are contained within small packets of fluid, with the size of these fluid packets increasing, and possibly becoming more coherent, as the Reynolds number increases and where the majority of the structure consists of either Q1 or Q4 events. The flow structure is subordinated, in terms of spatial coverage within these CFS, by Q1 events, which are located both at the base and the top front (tip) of the CFS. Directly above the CFS, a packet of Q2 events is also frequently detected. These observations agree with previous boundary layer studies where magnitude Q4 events tend to dominate [*Nelson et al.,* 1995], with Q2 and Q4 events extracting turbulent energy from the mean and they contribute to the bed shear stress.

When the turbulent kinetic energy (TKE) is analysed, several characteristics are identified. Firstly, high TKE can be observed within the CFS when it is close to the bed, potentially generated through shear, but the TKE diminishes with distance away from the bed. Furthermore, the location of the CFS follows defined trends. Primarily, the LIF dye is entrained at the end of a large structure that has passed through that region (Figure 2, T2, marked with dotted circle). This structure, detected by its high TKE, extends further into the flow (up to 0.5 z/h). These structures, especially those identified in the Re 46 500 experiment, appear to be generated by localised shear, where they entrain / coalesce with other turbulent structures moving upwards into the flow. However, as these CFS move away from the shear layer, they lose energy through entrainment and growth. These results may at first appear counterintuitive, as one of the definitions of a CFS given by *Adrian and Marusic* [2012] is that it contributes significantly to the hydraulic properties of a flow. However, the proposed mechanism which generates the CFS is ejected low-momentum fluid from a burst in the near-bed region [e.g. Grass *et al.,* 1971] and subsequently the products of the velocity components, namely the turbulent kinetic energy, contained with the flow structure will also be low. Finally, a region of high TKE is located behind the structure (Figure 2, T3), as demonstrated by quadrant analysis, and moves towards the bed, a characteristic that agrees with previous work that suggests Q2 events are replaced by an inrush of high velocity fluid from above [*e.g. Grass* 1971*; Grass et al.,* 1991*; Nezu and Nakagawa,* 1993*; Best*, 2005 *a&b*] (Figure 9).

The two dimensional (*x-z*) vorticity for all the CFS across the range of Reynolds numbers investigated herein generally shows weak positive vorticity, indicating a rolling motion generated from shear with the bed. However, as with the other flow components, closer inspection shows that each structure is not a single homogeneous flow structure, but rather comprises several vortices of both rotating and counter-rotating flow. This bears similarity to roller vortices formed in a classical boundary layer [e.g. *Adrian*, 2000] and is in agreement with the quadrant analysis presented herein. This observation provides insight into the potential formation and destruction mechanism of these CFS. Initially, positive vorticity suggests bed-shear induced processes for formation of these structures. However, as these flow structures do not form from a single topographic protrusion, such as a dune crest, but rather a multitude of three-dimensional topographic peaks, then consistently-sized vortices are not identified. Instead, a coalescence of several different scale vortices into the principal CFS is present. Additionally, these results provide insight into the dissipation of such CFS that are not permanent features and rarely stable: a small percentage of negative vorticity

suggests the CFS are already unstable and there is a transfer of energy to smaller eddies (e.g. the model of *Falco*, [1991]). The present results also confirm the criteria of *Adrian and Marusic* [2012] that these structures have regions that are ir/rotational.

The present study has also demonstrated that, independent of flow Reynolds number or track-period applied, the FTLE method can identify vortex chains originating at the bed and with a trajectory of between ≈35 to 45˚, similar to those structures identified by the LIF. Furthermore, a series of vortex chains are present higher in the flow that are reasoned to have been generated from topographic protrusions outside of the field of view. For all flow conditions, the greatest spatial agreement between the location of LIF and the high FTLE values corresponds with the longest (2s) track-back time following defined paths, with the LIF being entrained by vortex chains originating at the bed. For shorter track-back periods (0.5, 1s), the flow structure sits on high FTLE attractors that could either imply: i) that small structures, as identified in the vorticity, are spinning off a larger feature, or ii) that shear flow structures follow predefined flow paths from topographic protrusions in the bed and coalesce into these larger structures as they grow.

The PLIF-PIV technique detailed herein now permits future work that should investigate whether the generative mechanism for these bed-generated coherent flow structures is similar to the model proposed by *Wark and Nagib* [1991] They suggest merging hairpin vortices form around the bed clasts, and generate large 'roller-type' structures [*Townsend*, 1976; *Wark and Nagib*, 1991] or Kelvin-Helmholtz, roller-type, instabilities generated along the separation zone shear layer [e.g., *Rood and Hickin*, 1989; *Bennett and Best*, 1995; *Best*, 2005 *a&b*; *Hardy et al.,* 2009] that are formed around several anchor clasts in the bed. Furthermore, there is a need for such findings to be extended to examine how these turbulent flow structures influence the sediment transport dynamics [e.g. *Nikora and Goring*, 2000; *Shvidchenko and Pender*, 2001; *Maddux et al.,* 2003; *Nelson et al.,* 2005; *Yager and Schott*, 2013] and influence subsurface hyporheic flows [e.g. *Blois et al.,* 2014]. The relation between local turbulence and forces acting on the sediment grains is not understood and as such and there is still little agreement as to which turbulence statistic is the best descriptor to predict sediment entrainment [*Rennie and Millar*, 2004; *Schmeeckle et al*., 2007; *Wren et al*., 2007; *Coleman and Nikora,* 2008; *Paiement-Paradis et al*., 2011]. The mechanism which causes

sediment to be entrained is dominated by drag, lift or a product of both forces [*Vollmer and Kleinhans*, 2007; *Schmeekele et al.,* 2007; *Yager and Schott*, 2013] although the contribution from each component has yet to be fully quantified. The drag force can be correlated with the downstream velocity fluctuations, or near-bed Reynolds stresses [*Yager and Schott*, 2013], however, no such relation exists for the lift force which does not correlate with the local instantaneous vertical (*w*-) velocity [*Schmeeckle et al.*, 2007]. There is a better agreement between the localised pressure field, induced from flow around topographic protrusions and spatial accelerations, and the lift force [*Smart*, 2005; *Schmeeckle et al.,* 2007]. However, sustained fluctuations of turbulence may generate the forces needed for entrainment [*Yager and Schott*, 2013], and as such bursts (Q2), sweeps (Q4) and inward (Q3) and outward interactions (Q1) can cause significant sediment entrainment [*Grass*, 1970; *Nelson et al.*, 1995], with observations suggesting that Q4 and Q1 cause the most sediment transport because of their frequency [*Nelson et al.*, 1995]. Recent work [e.g. *Diplas et al.,* 2008; *Diplas and Dancy*, 2013] has also shown how sediment entrainment is a function of both the magnitude and duration of a turbulent event impacting on a bed surface, and thus highlights how the size, form and stacking of CFS into larger flow structures may be critical in sediment entrainment. For instance, the results presented herein demonstrate that high TKE is present in the flow structure when it is close to the bed, thus potentially providing the necessary energy for grain entrainment. The current analysis has also shown that as the flow Reynolds number increases, there is an increase in the percentage of the CFS containing Q4 events (>80%), with the next most dominant flow structures being Q1 events, which are located both at the base and front tip of the CFS. Even though all the flow conditions used in the current experiments were below the bed shear stresses required for sediment entrainment, the results imply that these structures may generate high instantaneous bed shear stresses that are the causal mechanism for sediment entrainment.

7. Acknowledgements

Editor Bruce MacVicar and three anonymous referees for providing helpful comments that have led to significant improvements in this manuscript.

8. References

Adrian, R. J. (2007), Hairpin vortex organization in wall turbulence, *Phys. Fluids, 19*, 041601.

Adrian, R. J. (2013), Structure of Turbulent Boundary Layers, In: *Coherent Flow Structures at Earth's Surface*, First Edition. Edited by Jeremy G. Venditti, James L. Best, Michael Church and Richard J. Hardy. John Wiley & Sons Ltd,17-24

Adrian, R. J. and I. Marusic, (2012), Coherent structures in flow over hydraulic engineering surfaces, *J. Hydraul. Res., 50*, 451–64.

Babakaiff, C. S. and E. J. Hickin, (1996), Coherent flow structures in the Squamish River estuary, BC, Canada, In: P.J. Ashworth, S.J. Bennett and S.J. McLelland (Eds), *Coherent Flow Structures*, Wiley, Chichester, 312-342

Bai J., H. Fang and T. Stoesser T. (2013), Transport and deposition of fine sediment in open channels with different aspect ratios, *Earth Surface Processes and Landforms*, *38 (6)*, 591-600.

Bathurst, J. C. (1978), Flow resistance of large scale roughness, *J. Hydraul. Div., ASCE, 104(HY12)*, 1587–603.

Bennett, S. J. and J. L. Best (1995), Mean flow and turbulence structure over fixed, two dimensional dunes: implications for sediment transport and dune stability, *Sedimentology, 42*, 491-513.

Best, J. L. (2005), The fluid dynamics of river dunes: A review and some future research directions, *J. Geophys. Res.*, doi:10.1029/2004JF000218.

Best, J. L. and R. A. Kostaschuk (2002), An experimental study of turbulent flow over a low-angle dune, *J. Geophys. Res., 107(C9)*, 3135,

Best, J. L. and A. G. Roy, (1991), Mixing layer distortion at the confluence of different depths, *Nature, 350 (6317)*, 411-13

Blois, G., J. L. Best, G. H. Sambrook Smith, and R. J. Hardy (2014), Effect of bed permeability and hyporheic flow on turbulent flow over bed forms, *Geophys. Res. Lett., 41*, doi:10.1002/ 2014GL060906.

Bogard, D. G. and W. G. Tiederman (1986), Burst detection with single-point velocity measurement, *J. Fluid Mech.*, *162*, 113-135.

Buffin-Bélanger, T. and A. G. Roy (1998), Effects of a pebble cluster on the turbulent structure of a depth-limited flow in a gravel-bed river, *Geomorphology, 25*, 249–67

Buffin-Belanger, T., A. G. Roy and A. D. Kirkbride (2000), On large scale flow structures in a gravel bed river, *Geomorphology, 32*, 417–35.

Cantwell, B. J. (1981), Organized motion in turbulent flow, *Ann. Rev. Fluid Mech., 13*, 457.

Charlton, F. G., P. M. Brown, and R. W. Benson (1978), The hydraulic geometry of some gravel rivers in Britain, Report IT180, Hydraulics Research Station, Wallingford, England.

Coleman, S.E. and V.I. Nikora, (2008), A unifying framework for particle entrainment. *Water Resour. Res.*, 44 (4), W04415.

Colombini, M. (1993), Turbulence driven secondary flows and the formation of sand ridges, *J. Fluid Mech., 254*, 701– 19.

Cooper J. R. and S. J. Tait, (2008), The influence of spatial variability in the near-bed flow field on 1-D calculations of fluvial bedload transport. In: River, Coastal and Estuarine Morphodynamics : RCEM 2007, Vols 1 and 2 Eds. Dohmen Janssen CM and Hulscher SJMH Proceedings and Monographs in Engineering, Water and Earth Sciences, 437-42

Cooper J. R. and S. J. Tait, (2010a), Spatially representative velocity measurement over water-worked gravel beds, *Water Resourc. Res., 46*, W11559

Cooper J. R. and S. J. Tait, (2010b), Examining the physical components of boundary shear stress for water-worked gravel deposits, *Earth Surfaces Process. Landforms, 35(10)*, 1240-6.

Crimaldi, J. P. and Koseff, J. R. (2001), High-resolution measurements of the spatial and temporal scalar structure of a turbulent plume, *Exp. Fluids*, *31*, 90–102.

Dinehart, R. L. (1992), Evolution of coarse gravel bed forms – Field measurements at flood stage, *Water Resourc. Res., 28(10)*, 2667–89.

Drake, T. G., R. L. Shreve, W. E. Dietrich, P. J. Whiting, and L. B. Leopold (1988), Bedload transport of fine gravel observed by motion-picture photography, *J. Fluid Mech., 192*, 193–217.

Diplas, P., Dancey, C.L., Celik, A.O., Valyrakis, M., Greer, K., and Akar, T., (2008), The role of impulse on the initiation of particle movement under turbulent flow conditions. Science, 322: 717-720,doi:10.1126/science.1158954.

Diplas, P. and C.L. Dancy, (2013), Coherent flow structures, initiation of motion, sediment transport and morphological feedback in rivers, In: *Coherent Flow Structures at Earth's Surface*, First Edition. Edited by Jeremy G. Venditti, James L. Best, Michael Church and Richard J. Hardy. John Wiley & Sons, Ltd, 289-308.

Falco, R.E. (1977), Coherent motions in the outer region of a turbulent boundary layers, *Physics of Fluids, 20*, s124–s132.

Falco R.E. (1991), A coherent structure model of the turbulent boundary layer and its ability to predict Reynolds number dependence, *Philosophical Transactions of the Royal Society of London Series-A Mathematical Physical and Engineering Sciences*, *336 (1641)*, 103-129.

Garcia, C., H. Cohen, I. Reid, A. Rovira, X. Ubeda, and J. B. Laronne (2007), Processes of initiation of motion leading to bed load transport in gravel bed rivers, *Geophys. Res. Lett., 34, L96403*.

Grass, A. J. (1971), Structural features of turbulent flow over smooth and rough boundaries, *J. Fluid Mech., 50*, 233–55.

Grass, A. J., R. J. Stuart, and M. Mansour-Tehrani (1991), Vortical structures and coherent motion in turbulent flow over smooth and rough boundaries, *Philos. Trans. R. Soc., Ser. A, 336*, 35 – 65.

Green M. A., C. W. Rowley and G. Haller (2006), Detection of Lagrangian coherent structures in three-dimensional turbulence, *J. Fluid Mech., 572*, 111–20

Haller, G. (2001), Distinguished material surfaces and coherent structures in 3D fluid flows. *Physica D, 149*, 248–77.

Haller, G. and G. Yuan (2000), Lagrangian coherent structures and mixing in two-dimensional turbulence, *Physica D*, *147(3–4)*, 352-70.

Hardy, R. J., S. N. Lane, M. R. Lawless, J. L. Best, L. Elliott, and D. B. Ingham (2005), Development and testing of a numerical code for treatment of complex river channel topography in three-dimensional CFD models with structured grids, *J. Hydraul. Res., 43*, 468–80.

Hardy, R. J., S. N. Lane, R. I. Ferguson, and D. R. Parsons (2007), Emergence of coherent flow structures over a gravel surface: A numerical experiment, *Water Resourc. Res., 43*, W03422, doi:10.1029/2006WR004936.

Hardy, R. J., J. L. Best, S. N. Lane, and P. E. Carbonneau (2009), Coherent flow structures in a depth-limited flow over a gravel surface: the role of nearbed turbulence and influence of Reynolds number, *J. Geophys. Res., 114, F01003*.

Hardy, R. J., J. L. Best, S. N. Lane, and P. E. Carbonneau (2010), Coherent flow structures in a depth- limited flow over a gravel surface: the influence of surface roughness, *J. Geophys. Res.*, *115*, F03006

Hardy, R.J., J. L Best, D .R. Parsons, and G. M Keevil, (2011)On determining the geometric and kinematic characteristics of coherent flow structures over a gravel bed: a new approach using combined PLIF-PIV, *Earth Surface Process. Landforms, 36(2*) 279-84

Heathershaw, AD (1974) Bursting phenomena in the sea, *Nature, 248(5447)*, 394-5

Horner-Devine A. R., C. Chickadel, and D.G. MacDonald, (2013) Coherent Structures and Mixing at a River Plume Front, In: *Coherent Flow Structures at Earth's Surface*, First Edition. Edited by Jeremy G. Venditti, James L. Best, Michael Church and Richard J. Hardy. John Wiley & Sons, Ltd, 359-70.

Hunt, J. C. R., A. A. Wray, and P. Moin, (1988), Eddies, stream, and convergence zones in turbulent flows, Centre for Turbulence Research Rep. CTR-S88.

Imamoto, H., and T. Ishigaki (1986a), The three dimensional structure of turbulent shear flow in an open channel, paper presented at Fifth Congress of the Asian and Pacific Regional Division of the International Association for Hydraulic Research, Seoul.

Imamoto, H., and T. Ishigaki (1986b), Visualization of longitudinal eddies in an open channel flow, in Flow Visualization IV: Proceedings of the Fourth International Symposium on Flow Visualization, edited by C. Veret, pp. 333– 337, Hemisphere, Washington, D.C.

Jackson, R. G. (1976), Sedimentological and fluid-dynamic implications of the turbulent bursting phenomenon in geophysical flows, *J. Fluid Mech., 77*, 531–60.

Jessup A.T., C. Chickade S.A. Talke and A.R. Horner-Devine, (2013) COHSTREX: Coherent Structures in Rivers and Estuaries Experiment, In: *Coherent Flow Structures at Earth's Surface*, First Edition. Edited by Jeremy G. Venditti, James L. Best, Michael Church and Richard J. Hardy. John Wiley & Sons, Ltd, 215-30.

Klaven, A. B. (1966), Investigation of the flow turbulent structure (in Russian), *Trans. State Hydrol. Inst., 136*, 65–76.

Klaven, A. B., and Z. D. Kopaliani (1973), Laboratory investigations of the kinematic structure of turbulent flow over a rough bed (in Russian), *Trans. State Hydrol. Inst., 209*, 67–90.

Kline S. J., W.C. Reynolds, F.A .Schraub, and P.W. Runsstadl, (1967), Structure of turbulent boundary layers, *J. Fluid Mech., 30*, 741.

Kostaschuk, R. A. and M. A. Church, (1993), Macroturbulence generated by dunes: Fraser River, Canada. *Sedimentary Geology, 85*, 25–37.

Krogstad P.A., R.A. Antonia and L.W.B. Browne (1992), Comparison between rough- and smooth-wall turbulent boundary layers. *J. Fluid Mech.*, 245, 599-617.

Lacey R. W and A. G. Roy (2006), Turbulent wake region of large roughness elements: Combining flow visualization and high frequency velocity measurements, In: River Flow 2006, Vols 1 and 2 Eds Ferreira, RML; Alves, CTL; Leal, GAB; Cardoso, AH Proceedings and Monographs in Engineering, Water and Earth Sciences 125-34

Lacey, R. W. J., P. Legendre and A. G. Roy (2007), Spatial scale partitioning of in situ turbulent flow data over a pebble cluster in a gravel-bed river, *Water Resourc. Res., 43*, W03416.

Lacey R. W. and A. G. Roy (2008), The spatial characterization of turbulence around large roughness elements in a gravel-bed river, *Geomorphology, 102(3-4)*, 542-53

Lamarre H. and A. G. Roy, (2005), Reach scale variability of turbulent flow characteristics in a gravel-bed river, *Geomorphology, 68(1-2)*, 95-113

Lu, S. S., and W. W. Willmarth (1973), Measurements of structure of Reynolds Stress in a turbulent boundary layer, *J. Fluid Mech., 60,* 481-511.

MacVicar B. J. and A. G. Roy (2007a), Hydrodynamics of a forced riffle pool in a gravel bed river: 1. Mean velocity and turbulence intensity, *Water Resourc. Res., 43(12)*

MacVicar B. J. and A. G. Roy (2007b), Hydrodynamics of a forced riffle pool in a gravel bed river: 2. Scale and structure of coherent turbulent events, *Water Resourc. Res.*, *43(12)*, W12402

Maddux, T. B., J. M. Nelson, and S. R. McLean (2003), Turbulent flow over three-dimensional dunes: 1. Free surface and flow response, *J. Geophys. Res*., 108(F1), 6009.

Marquis, G. A., and A. G. Roy (2006), Turbulent processes at the entrance of a pool using flow visualization, in *River Flow 2006*, edited by R. M. L. Ferreira, pp. 109–17, Taylor and Francis, London.

Marquis G. P. and A .G. Roy (2011), Effects of turbulence on the transport of individual particles as bedload in a gravel-bed river, *Earth Surface Process. Landforms, 36(1)*, 107-16.

Marquis G.A. and A. G. Roy, (2013), From Macroturbulent Flow Structures to Large-Scale Flow Pulsations in Gravel-Bed Rivers, , In: *Coherent Flow Structures at Earth's Surface*, First Edition. Edited by Jeremy G. Venditti, James L. Best, Michael Church and Richard J. Hardy. JohnWiley & Sons, Ltd, 261-274.

Mejia-Alvarez, R., J. M. Barros and K.T. Christensen, (2013), Structural attributes of turbulent flows over a complex topography, In: *Coherent Flow Structures at Earth's Surface*, First Edition. Edited by Jeremy G. Venditti, James L. Best, Michael Church and Richard J. Hardy. JohnWiley & Sons, Ltd, 25-42.

Müller, A., and A. Gyr (1982), Visualisation of the mixing layer behind dunes, in *Mechanics of Sediment Transport* edited by B. M. Summer and A. Müller, pp. 41-45, Balkema, Rotterdam.

Nelson J. M., R. L. Shreve, S. R. McLean and T. G. Drake (1995), Role of near-bed turbulence structure in bed load transport and bed form mechanics, *Water Resourc. Res., 31*, 2071-2086.

Nelson, J., A. R. Burman, Y. Shimizu, S. R. McLean, R. L. Shreve, and M. W. Schmeeckle (2005), Computing of and sediment transport over bedforms, *Proc. of Int. Conf. On Riv. Coast. and Est. Morph., RCEM,* 861-868.

Nezu, I., and H. Nakagawa (1993), Turbulence in Open Channel Flows, A. Balkema, Rotterdam, Netherlands. 286 pp

Nikora, V. I. and D. G. Goring (2000), Flow turbulence over fixed and weakly mobile gravel beds, *J. Hydraul. Div., ASCE, 126(9)*, 679-90.

Nikora, V. and Roy, A.G. (2012) Secondary Flows in Rivers: Theoretical Framework, Recent Advances, and Current Challenges In *Gravel Bed Rivers: Processes, Tools, Environments* Eds M Church, P. Biron and A.G., Roy, Wiley. 3-22

Nowell, A. R. M., and M. Church (1979), Turbulent flow in a depth limited boundary layer, *J. Geophys. Res., 84 (C8)*, 4816-4824.

Otsu N. (1979), A threshold selection method from gray-level histograms, *IEEE Transactions, Systems, Man and Cybernetics, 9,* 62–6

Paiement-Paradis G., T. Buffin-Belanger A.G. Roy (2003), Scalings for large turbulent flow structures in gravel-bed rivers, *Geophys. Res. Lett., 30*, 1773.

Rennie, C. D. and R.G.Millar, (2004), Measurement of the spatial distribution of fluvial bedload transport velocity in both sand and gravel. *Earth Surface Processes and Landforms*, *29*, 1173-93.

Robert, A., A. G. Roy, and B. De Serres (1992), Changes in velocity profiles at roughness transitions in coarse grained channels, *Sedimentology*, 39, 725–35

Robinson, S. K. (1991) Coherent motions in the turbulent boundary layer, *Annu. Rev. Fluid Mech., 23*, 601–39

Rodriguez, J.F. and M.H. Garcia, (2008), Laboratory measurements of 3-D flow patterns and turbulence in straight open channel with rough bed. *J. of Hydraulic Res*., *46(4)*, 454-45.

Roy A. G, P. M. Biron, T. Buffin-Belanger , M. Levasseur M. (1999), Combined visual and quantitative techniques in the study of natural turbulent flows. *Water Resourc. Res., 35*, 871–77

Roy A. G., and T. Buffin-Bélanger (2001), Advances in the study of turbulent flow structures in gravel-bed rivers, in *Gravel-Bed Rivers V*, Ed M.P. Mosley, pp. 375-404, NZ Hydrological Society.

Roy, A. G., P. M. Biron, T. Buffin-Bélanger, and M. Levasseur (1999), Combined visual and quantitative techniques in the study of natural turbulent flows, *Water Resourc. Res., 35*, 871-7.

Roy, A.G, T. Buffin-Belanger, H. Lamarre, A.D. Kirkbride (2004), Size, shape and dynamics of large-scale turbulent flow structures in a gravel-bed river, *J. Fluid Mech., 500*, 1–27.

Roy, M. L., A.G. Roy, and P. Legendre, (2010), The relations between 'standard' fluvial habitat variables and turbulent flow at multiple scales in morphological units of a gravel bed river, *River Research and Applications, 26*, 439-55.

Schmeeckle, M.W., J. M., Nelson and R. L Shreve, (2007), Forces on stationary particles in near-bed turbulent flows. *J. Geophys. Res., 112*(F2), F02003

Shen, C., and U. Lemmin (1999), Application of an acoustic particle flux profiler in particle laden open channel flow, *Journal of Hydraul. Res., 37*, 407–19.

Shiono K. T. and Feng, (2003), Turbulence measurements of dye concentration and effects of secondary flow on distribution in open channel flows, *J. Hydraul. Div., ASCE, 129(5)*, 373–84.

Shvidchenko, A., and G. Pender (2001), Macroturbulent structure of open channel flow over gravely beds, *Water Resourc. Res., 37*, 709–19.

Simpson, R. L. (1989), Turbulent boundary layer separation, *Annu. Rev. Fluid Mech., 21*, 205–34.

Singh, A. and E. Foufoula-Georgiou, (2013), Effect of Migrating Bed Topography on Flow Turbulence: Implications for Modelling Sediment Transport, In: *Coherent Flow Structures at Earth's Surface*, First Edition. Edited by Jeremy G. Venditti, James L. Best, Michael Church and Richard J. Hardy. by JohnWiley & Sons Ltd, 323-40.

Socolofsky, S. A., and G. H. Jirka (2004), Large scale flow structures and stability in shallow flows, *Journal of Environmental Engineering and Science, 3(5)*, 451–62.

Sukhodolov, A. N., and Rhoads, B. I. (2001), Field investigation of three dimensional flow structure at stream confluences, *Water Resourc. Res., 37*, 2411-24.

Talmon, A. M., J. M. G. Kunen, and G. Oooms (1986), Simultaneous flow visualization and Reynolds stress measurement in a turbulent boundary layer, *J. Fluid Mech., 163*, 459–78.

Tamburrino and J. S. Gulliver, (1999), Large flow structures in a turbulent open channel flow, *Journal of Hydraul. Res*., *37(3)*, 363-80.

Tominaga, A., I. Nezu and S. Kobatake, (1989), Flow measurements in compound channels with a fiber optic laser Doppler anemometer. *I.A.H.R. Workshop on Instrumentation for Hydr. Laboratories,* Canada Centre for Inland Waters, Burlington, Ontario, Canada, 45-59.

Townsend A.A. (1976), The structure of turbulent shear flow, 2nd eds. Cambridge University press.

Van Dyke, M., (1982), An Album of Flow Visualisation1, Parabolic, Stanford, Calif. 76 pp.

Venditti, J.G., and S.J. Bennett, (2000), Spectral analysis of turbulent flow and suspended sediment transport over fixed dunes, *J. Geophys. Res*.,*105*, 22035–47

Vendetti J.G., R.J.Hardy, M. Church, M and J.L Best, (2013), What is a Coherent Flow Structure in Geophysical Flow?, In: *Coherent Flow Structures at Earth's Surface*, First Edition. Edited by Jeremy G. Venditti, James L. Best, Michael Church and Richard J. Hardy. JohnWiley & Sons Ltd, 1-16

Vollmer, S. and M.G. Kleinhans, (2007), Predicting incipient motion, including the effect of turbulent pressure fluctuations in the bed, *Water Resourc. Res*., **43** W05410.

Wark, C.E., and H.M. Nagib, (1991), Experimental Investigation of Coherent Structures in Turbulent Boundary Layers, *J. Fluid Mech., 230*, 183-208.

Webster, D. R, S. Rahman and L. P. Dasi (2003), Laser-Induced Fluorescence Measurements of a Turbulent Plume, *J. Engin. Mech., 129(10),* 1130-1137,

Westerweel, J. (1997), Fundamental of digital particle image velocimetry, *Meas. Sci. Technol., 8*, 1379–92.

Wilbert, C. and M. Gharib (1991), Digital particle image velocimetry, *Exp.Fluids, 10*, 181–93.

Wiberg, P. L. and J. D. Smith (1991), Velocity distribution and bed roughness in high-gradient streams, *Water Resourc. Res., 27*, 825 –38

Wren D.G., R.A. Kuhnle and C.G. Wilson (2007) Measurements of the relationship between turbulence and sediment in suspension over mobile sand dunes in a laboratory flume, *J. Geophys. Res.,* **112**, F03009.

Yalin, M. S. (1992), *River Mechanics*, 219 pp., Pergamon Press, Oxford, U.K.

Zaitsev, N. I. (1984), Large-scale structure of turbulent flow in a rectangular flume (in Russian), *Trans. State Hydrol. Inst., 318*, 3–17

Zhou, J., R. J. Adrian, S. Balachandar and T. M. Kendall, (1999), Mechanisms for generating coherent packets of hairpin vortices in channel flow, *J. Fluid Mech., 387*, 385–96.

Table 1: Summary of the experimental conditions calculated from the range of variables presented in the present and three previous studies. Where D_{50} is the median size, h is the flow depth used in the experiments, Re is the Reynolds number and Fr is the Froude number. The abreviations for the sources refer to; PS the present study; S&P [2001] to Shvidchenko and Pender [2001]; K&K [1973] to Klaven and Kopaliani [1973]; and I&I [1986a] to Imamoto and Ishigaki [1986a].

Source	D_{50} (mm)	h (m)	D_{50}/h	Velocity (ms^{-1})	Re ($\times 10^3$)	Fr
PS	44	0.3	0.15	0.08-0.58	19-132	0.04-0.4
S&P [2001]	2.14-7.15	0.025-0.107	0.22-0.286	0.41-0.98	8-80	0.4-0.95
K&K [1973]	3-14	0.05-0.052	0.58-0.27	0.54-0.56	20-22	0.8
I&I [1986a]	12	0.04	0.3	0.19	6	0.3
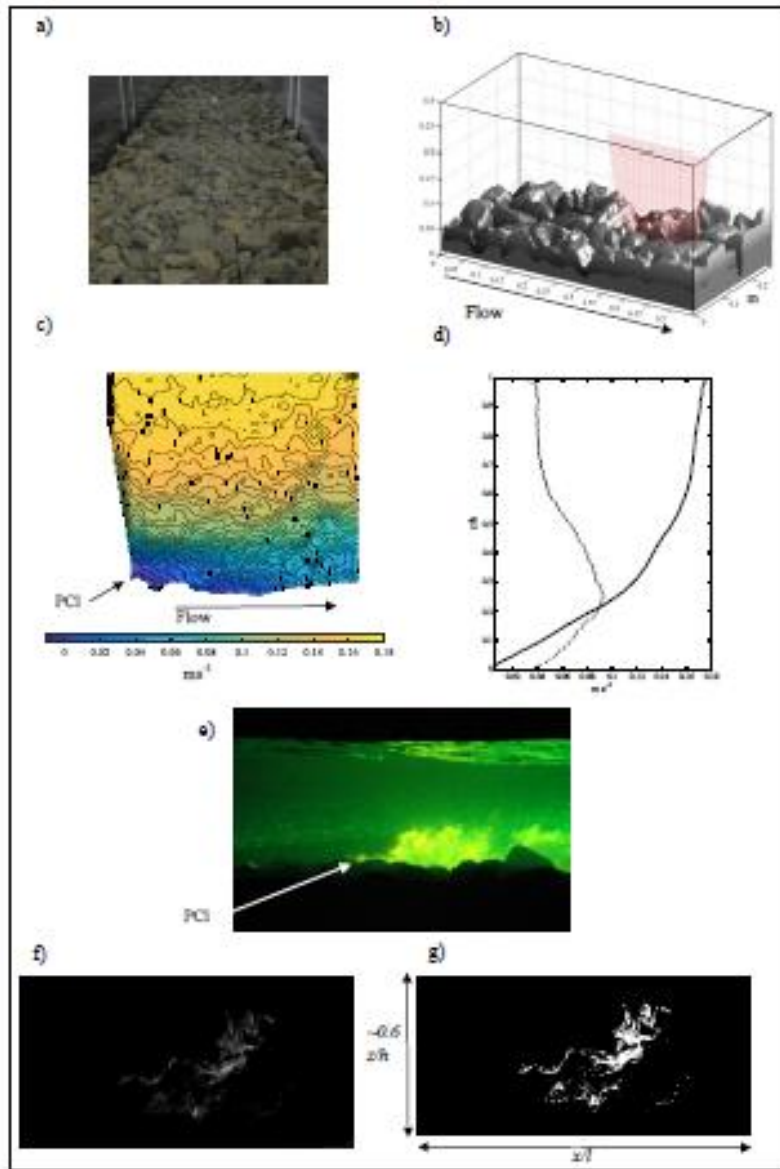
Figure 1: *The experimental set up: a) the gravel in the flume. The grain size distribution has a D_{50} of 44 mm and a D_{84} of 66 mm; b) A DEM collected through Terrestrial Laser Scanning. The red shaded area demonstrates the area illuminated by laser; c) The mean downstream (u-) velocity component for the Re 132 000 experiment demonstrating the whole flow measurement with the PIV; d) An example of a mean velocity (solid line) and turbulence intensity (dotted line) profile extracted from the Re 132 000 experiment e) a side on view of the flume where the flow is illuminated by the laser, PIV seeding is illuminated and the coherent flow structures can be identified by the Rhodamine 6G dye; f) a raw LIF image. Length of abscissa axis is equal to 0.35 metres whilst the ordinate axis is equal to 0.285 meters. g) An example of the conversion of a raw LIF image into a binary image using the Otsu (1979) image conversion algorithm, which determines the mask for the coherent turbulent flow structure PIV data. PCl in c and f identify the protruding clast.*
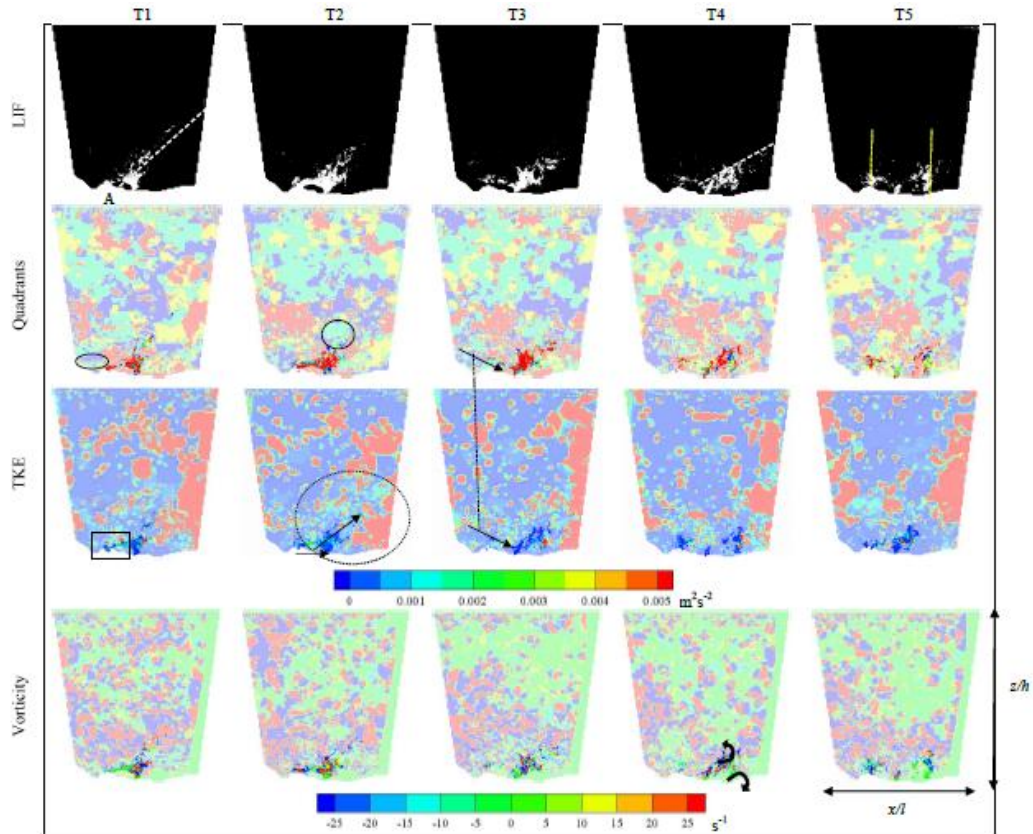
Figure 2: *A time series of images 0.06 seconds apart taken from the flow conditions of Re 132 000. The identified flow structure is shown through processed (binary) images in row 1. Flow is analysed through i) Instantaneous non-threholded quadrants (Q1 (Outward Interactions) blue; Q2 (Ejections) green; Q3 (Inward Interactions) yellow; & Q4 (sweeps) red), (Row 2); ii) Turbulent Kinetic Energy (TKE), (Row 3) and; iii) Vorticity (x-z) (Row 4) where the flow structure is in full colour and the surrounding flow has been plotted with 70% translucency. The lines, arrows, and ellipses identify regions of the flow discussed in detail in the text. The flow is from left to right.*
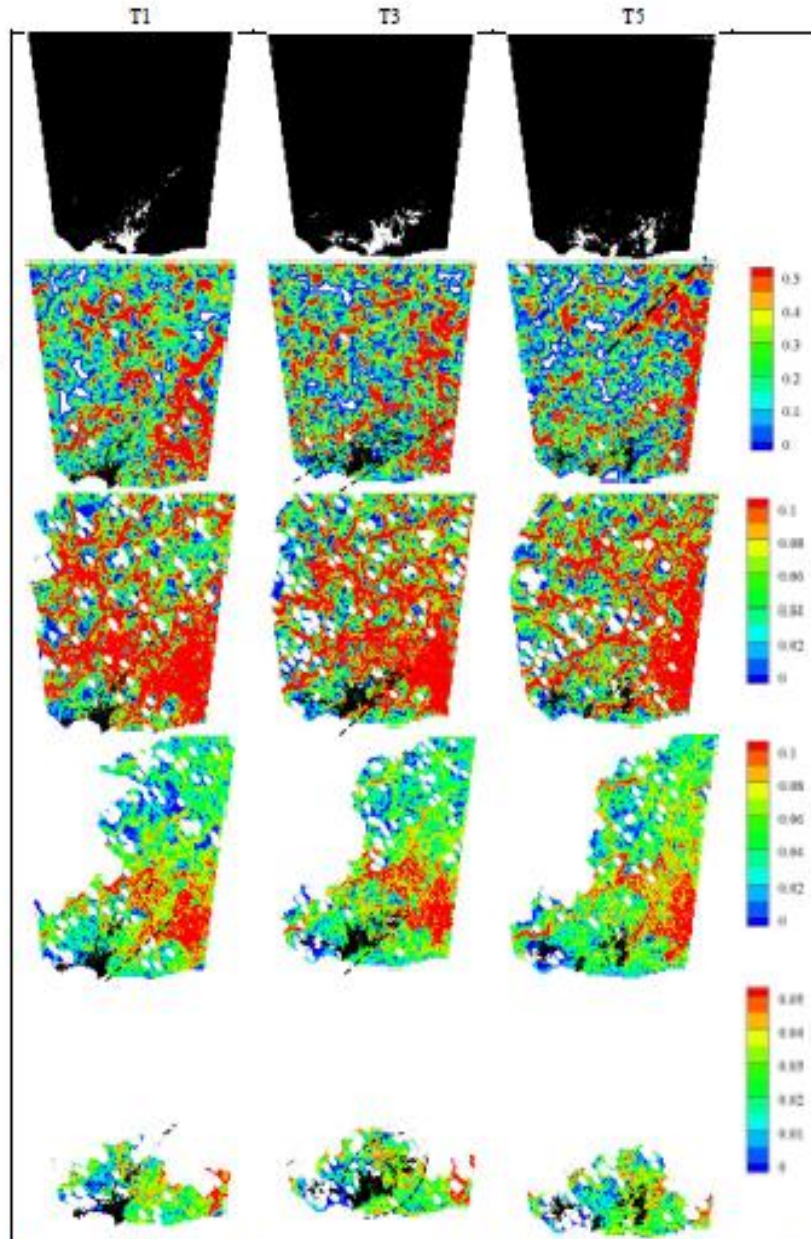
Figure 3: *Finite-time Lyapunov exponents (FTLE) plots for T1, T3 and T5 (as shown in Figure 2) for the Re 132 000 experiment. The identified flow structure is shown through processed (binary) images in row 1. The FTLE is shown with a track back of 0.05 s (row2), 0.5 s (row3), 1 s (row3) and 2s (row4). The CFS is shown in black in the FTLE images, while the blank area shows either areas where no significant structures are identified. The lines and ellipse identify regions of the flow discussed in detail in the text. The flow is from left to right.*
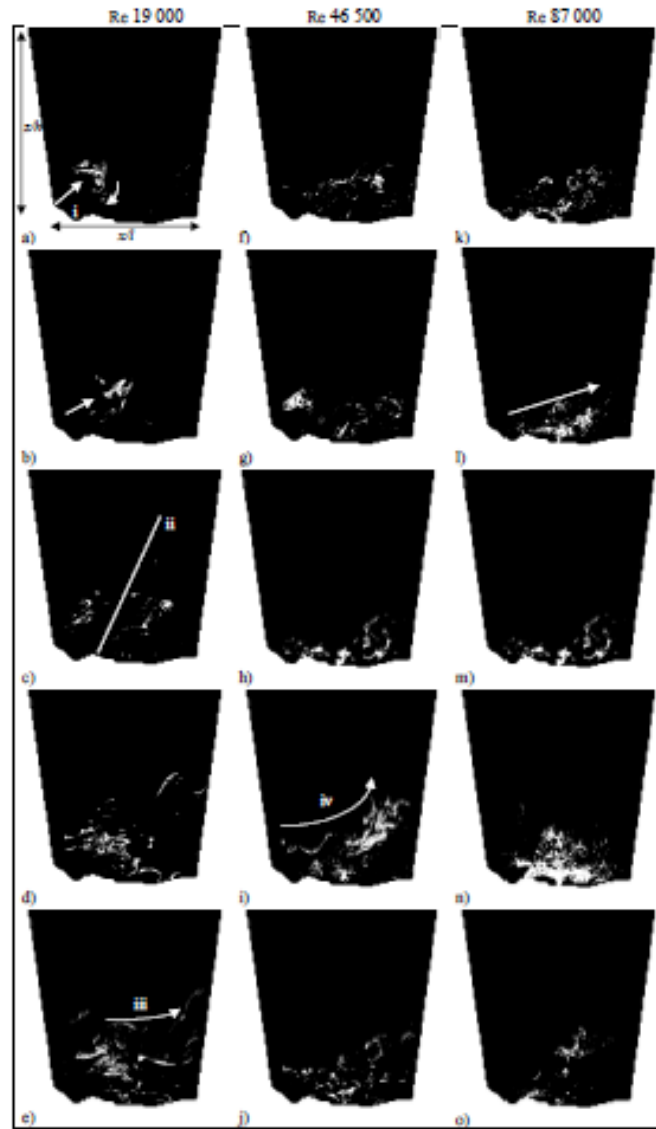
Figure 4: *A series of CFS detected by the LIF for the Re 19 000 (a-e), the Re 46 500 (f-j) and the Re 87 000 experiment (k-o). The images have been converted into binary using the Otsu (1979) algorithm. The lines and arrows identify regions of the flow discussed in detail in the text. The flow is from left to right.*
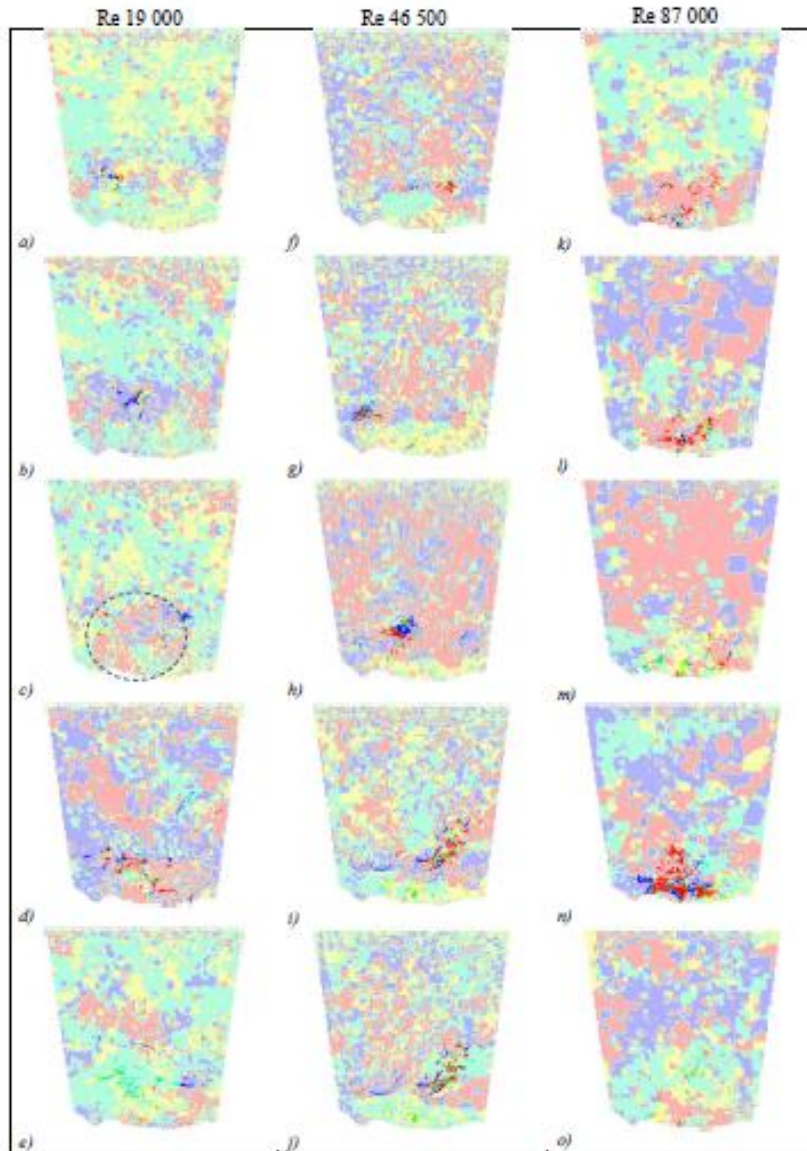
Figure 5: *Quadrant plot for the Re 19 000 (a-e), the Re 46 500 (f-j) and the Re 87 000 experiment (k-o). The full illumination is the identified flow structure, while the 70 % translucent image is the rest of the flow field. The flow structures used are those identified in Figure 4. Quadrant 1 (Outward Interactions) = Blue; Quadrant 2 (Ejections)= Green; Quadrant 3 (Inward Interactions)= Yellow; Quadrant 4 (Sweeps)= Red. The ellipse identifies regions of the flow discussed in detail in the text. The flow is from left to right.*
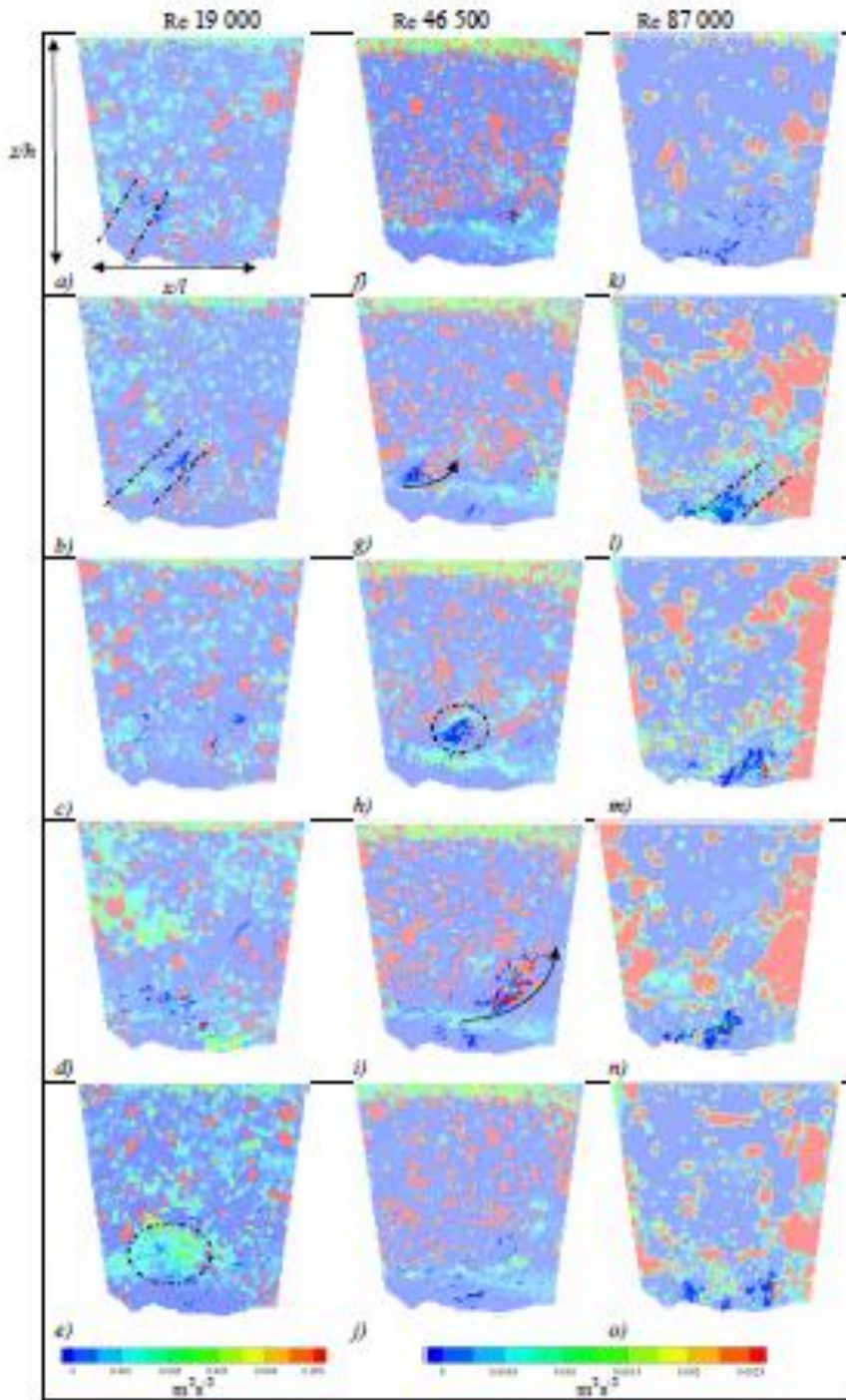
Figure 6: *Turbulent Kinetic Energy for the Re 19 000 (Column 1), the Re 46 500 (Column 2) and the Re 87 000 experiment (Column 3). The full illumination is the identified flow structure, while the 70% translucent image is the rest of the flow field. The flow structures used are those identified in Figure 4. z/h and x/l represents the dimensional height and length of the field of view. The lines, arrows, and ellipses identify regions of the flow discussed in detail in the text. The flow is from left to right.*
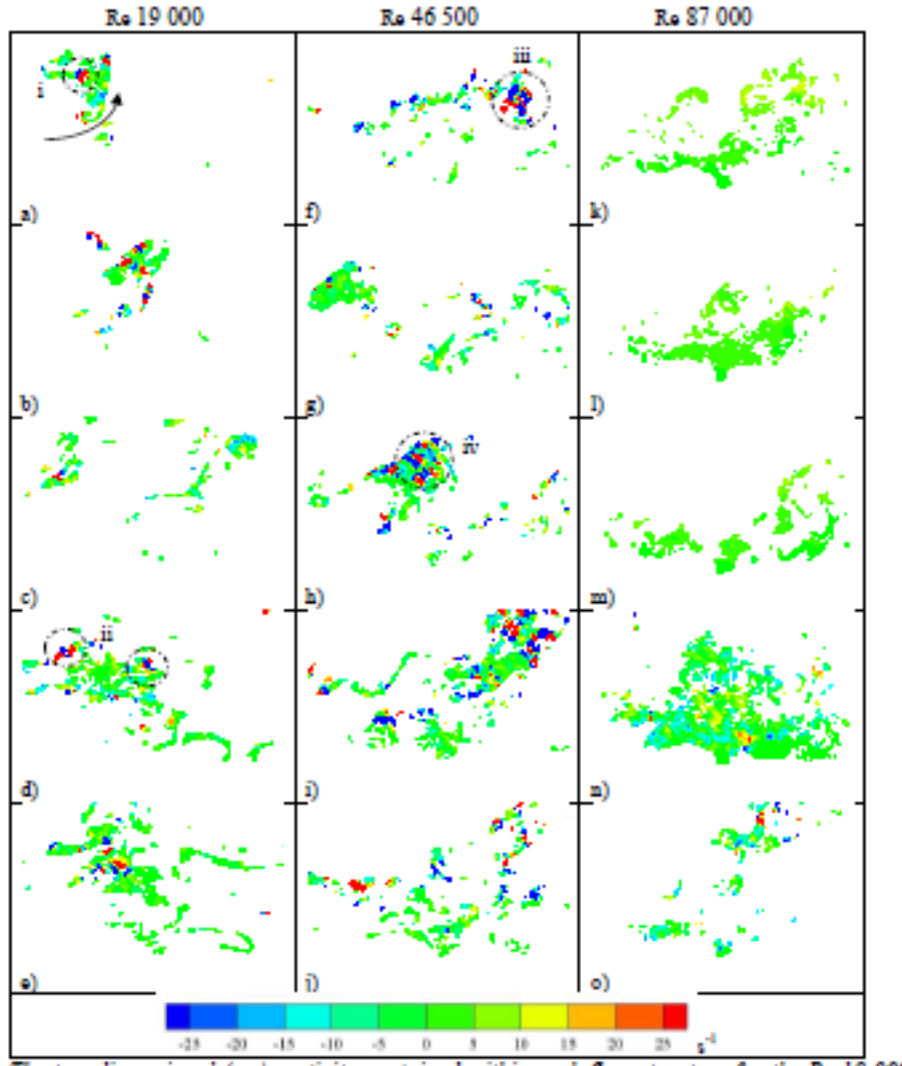
Figure 7: *The two dimensional (x-z) vorticity contained within each flow structure for the Re 19 000 (a-e), the Re 46 500 (f-j) and the Re 87 000 experiment (k-o). The flow structures used are those identified in Figure 4. The images have been cropped in order to identify local vorticity and the relative scale of the structure can be seen in Figure 4. The arrows, and ellipses identify regions of the flow discussed in detail in the text. The flow is from left to right.*
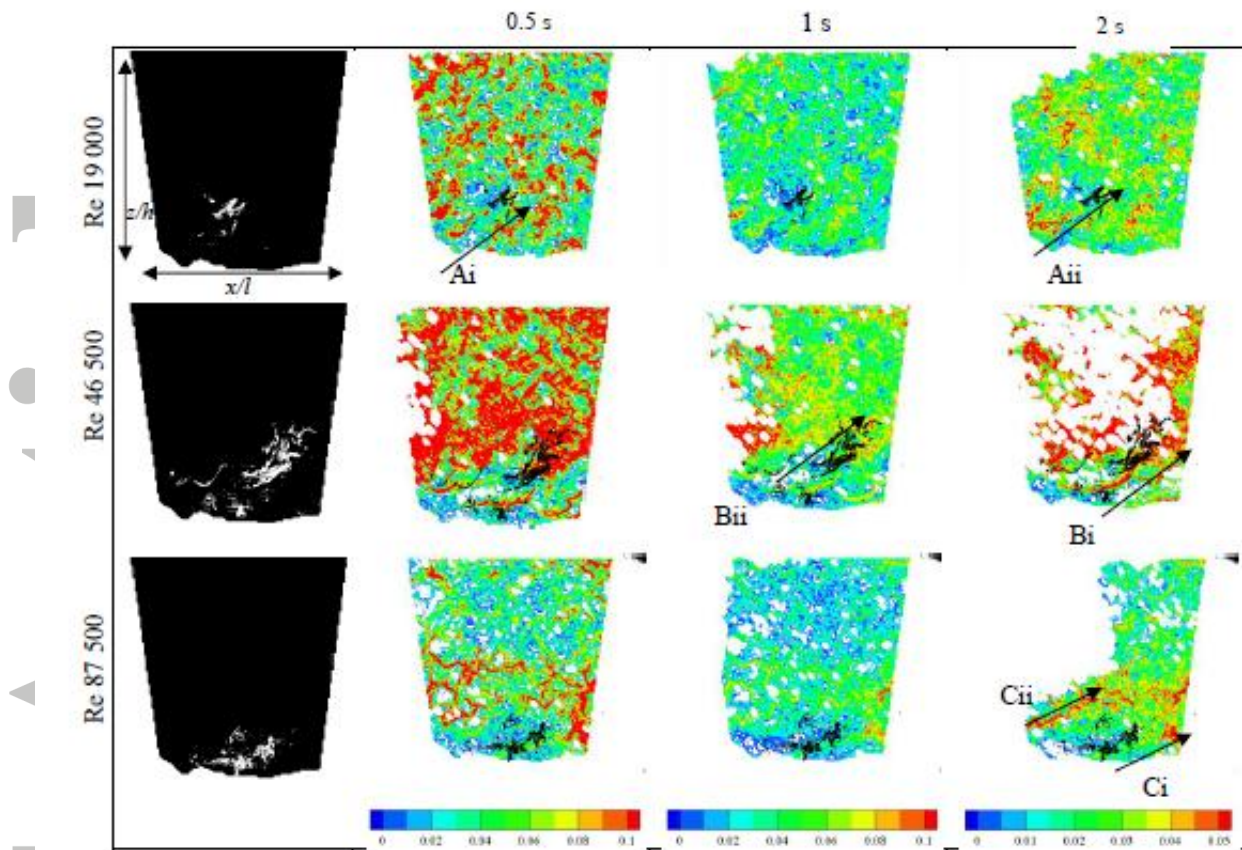
Figure 8: *Vortex detection using FTLE for selected flow structures. The structure is shown (Column 1) and then tracked back using FTLE for 0.5 seconds (Column 2), 1 second (Column 3) and 2 seconds (Column 4) for the Re 19 000 experiment (Row 1), Re 46 500 experiment (Row 2) and Re 87 500 experiment (row 3). The images chosen (column 1) have been previously analysed and correspond to: Re 19 000 (Figure 4b); Re 46 500 (Figure 4i) and; Re 87 500 (Figure 4l). The blank area shows either areas where no significant structures are identified. z/h and x/l represents the dimensional height and length of the field of view. The lines, arrows, and ellipses identify regions of the flow discussed in detail in the text. The flow is from left to right.*
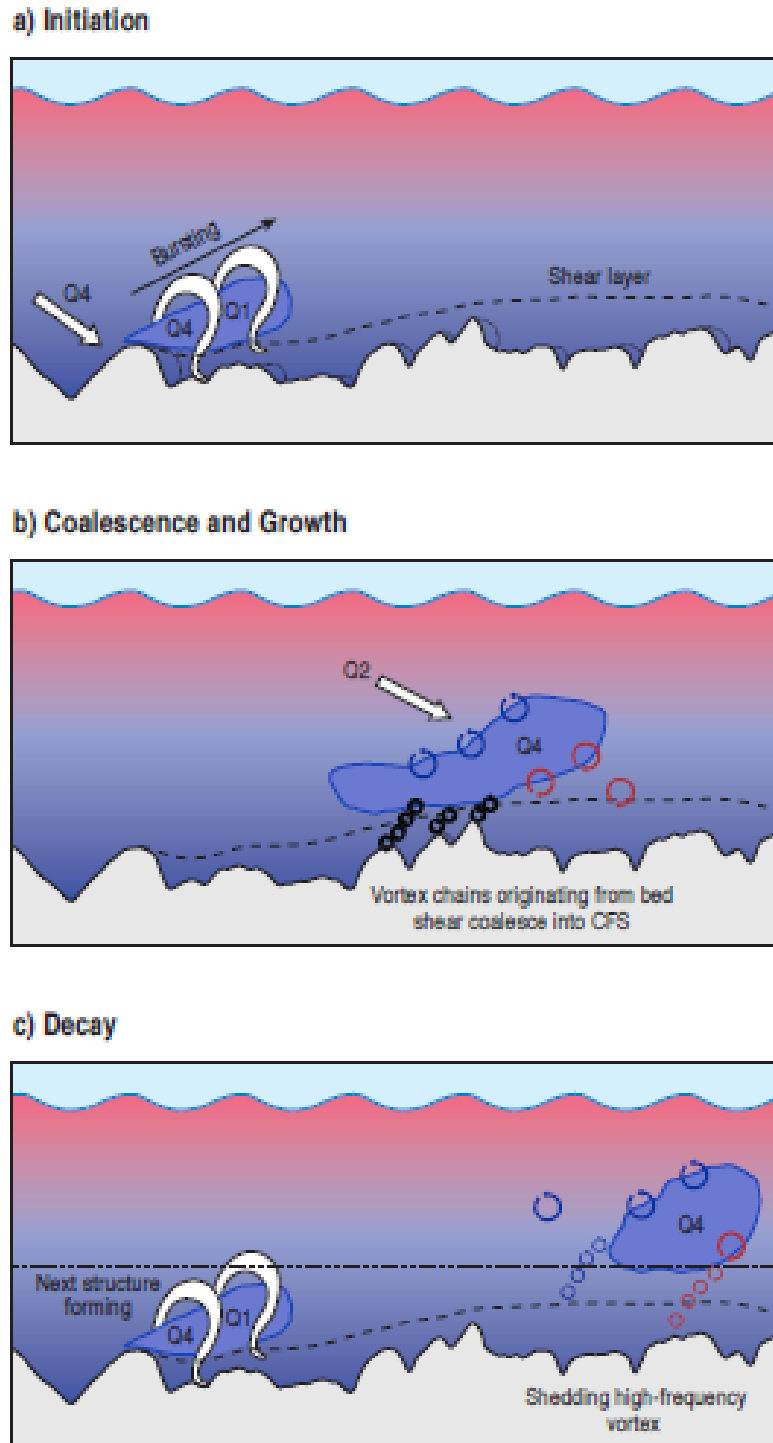
Figure 9: *A conceptual model for the initiation (A), growth (B) and decay (C) of a large-scale coherent flow structure over a gravel bed. The black line represents the topography used in the experiments, while the black dashed line represents the shear layer formed through the interaction with the large topographic protrusion to the left of the cartoon, and as previously observed in Hardy et al. [2009]. The CFS detected by the LIF is coloured blue; red arrows represent clockwise vorticity; blue arrows represent anticlockwise vorticity; black arrows represent vortex chains, with their diameter being a schematic indication of their size. Q refers to the dominant quadrant structure identified following the definition of Lu and Willmarth [1972]. Initiation of the structure (A) occurs through generation of horseshoe-*

shaped vortices in the shear flow linked to flow separation over the topographic protrusion. High turbulent kinetic energy is generated through shear in the near-bed region, although the flow structure does not lift away from the bed instantaneously. The dotted lines behind individual clasts show localized separation cells in the near bed region. The CFS grows (B) and moves away from the bed, with turbulent kinetic energy being fed to the structure through vortex chains originating at the bed. However, the life span of these structures is short in space and time and high frequency small vortices are sheared off the large structure as it breaks up and decays (C). Note that vortex evolution from only one topographic protrusion is highlighted, and in reality the bed will contain many such zones and their flow fields will interact creating a feedback between upstream-generated structures and downstream CFS initiation, evolution and decay.